metals

MDPI

Article

Effect of Annealing and Hot Isostatic Pressing on the Structure and Hydrogen Embrittlement Resistance of Powder-Bed Fusion-Printed CoCrFeNiMn High-Entropy Alloys

Shulu Feng [1,2], Zhijiu Ai [1,*], Jiayi He [2], Bangjian Yang [3], Guoqing Gou [3] and Lei Han [2]

[1] College of Mechanical and Electrical Engineering, Southwest Petroleum University, Chengdu 610500, China
[2] Petro China Southwest Pipeline Company, Chengdu 610094, China
[3] Key Laboratory of Advanced Materials Technology Ministry of Education, Southwest Jiaotong University, Chengdu 610031, China
* Correspondence: aizhijiuswpu@163.com

Abstract: As an additive-manufacturing (AM) technique, powder-bed fusion (PBF) shows tremendous potential in both the research and industrial communities. Research on the post-treatment of PBF-prepared products is a hot topic. Hydrogen embrittlement (HE) resistance is a practical necessity, especially in microstructures. Here, the effect of annealing and hot isostatic pressing (HIP) on the properties of PBF technology-printed CoCrFeNiMn high-entropy alloys (HEAs) is investigated. The results show that these two post-thermal treatment approaches can release residual stress (from approximately 338 to 44 MPa) from PBF-printed samples, which is the main reason for declines in hardness (from approximately 211 to 194 HV). In addition, both annealing and HIP can reduce HE sensitivity, thus improving resistance to HE, with elongation increasing by 75.4% and 85.4% after annealing and HIP, respectively. In summary, both post-thermal treatments are of great significance to the development of HEAs with optimized structures and protection against HE, which can contribute to the development of these behaviors during application.

Keywords: powder-bed fusion; high-entropy alloy; post-thermal treatments; residual stress; hydrogen embrittlement resistance

Citation: Feng, S.; Ai, Z.; He, J.; Yang, B.; Gou, G.; Han, L. Effect of Annealing and Hot Isostatic Pressing on the Structure and Hydrogen Embrittlement Resistance of Powder-Bed Fusion-Printed CoCrFeNiMn High-Entropy Alloys. *Metals* **2023**, *13*, 630. https://doi.org/10.3390/met13030630

Academic Editors: Gilbert Henaff and Jayaraj Jayamani

Received: 7 January 2023
Revised: 13 March 2023
Accepted: 15 March 2023
Published: 22 March 2023

1. Introduction

In recent years, the progress in additive manufacturing (AM) for processing high-entropy alloys (HEAs) has increasingly attracted attention in both the fields of academia and engineering [1–5]. Powder-bed fusion (PBF) printing technology possesses great potential for manufacturing HEA products with superior mechanical properties, thereby motivating their mass production for engineering applications. Furthermore, in respect of metal manufacturing, PBF is increasingly being employed due to its high degree of fabrication freedom without the use of other part-specific supplies, short design and fabrication periods, and the revolution of conventional manufacturing technologies in realizing an immense amount of time saved and low commercial costs [6–8]. In short, not only does PBF manufacturing not require extra devices, but it is also not restricted by complex part geometry, giving rise to multitudinous advantages, such as speediness, a short production period, and low cost [9–13].

Recently, HEAs have become a research hotspot in the field of alloys [14], because their high-mixing configurational entropies can help to stabilize solid solutions consisting of simple underlying face-centered cubic (FCC), body-centered cubic (BCC), or hexagonal close-packed (HCP) structures [5]. Due to the high diversity of constituent elements, achieved by means of tuning the chemical constituent elements and their proportions, various kinds of HEAs have shown superior mechanical characteristics, such as ductility, fracture toughness, superparamagnetic properties, superconductivity, and exceptional

irradiation resistance [15–19]. Hence, HEAs are excellent potential candidates for practical applications such as aero-engines, hard coatings on cutters, and components of fourth-generation nuclear reactors in extreme environments.

As materials with great engineering application and scientific research value, high-entropy alloys have gradually become a popular favorite, especially considering their wide application in various types of equipment and scenarios, such as in the long-distance and high-pressure transmission of oil and natural gas pipelines [20,21], welding processes [22], nuclear power plants [23], and in the humid environment industry [24,25]. Recently, a large amount of research has concentrated on the design principles, structure, and properties of HEAs processed using the PBF method, which combines both the advantages of state-of-the-art manufacturing technology and the inherent superior properties of HEAs, providing a befitting method to produce high-performance HEAs. However, the research on the additive manufacturing of CoCrFeNiMn HEA via PBF is still forthcoming. Compared to the conventional electric melting process, there is quite a difference in the solidification process and microstructure evolution of CoCrFeNiMn HEA powder in the formation process; meanwhile, many basic theoretical bases and technical points are still unclear. In addition, some inherent defects in PBF-printed HEAs still exist, such as inevitable pores, cracks, and nonuniformity that induce some deterioration of mechanical properties, seriously affecting premature failure in engineering applications [26,27]. Most importantly, hydrogen embrittlement susceptibility produced by the formation of microstructural defects such as dislocation, grain boundaries (GBs), twin boundaries (TBs), and interfaces are key factors to the occurrence of sudden brittle fracture [25,28–30]. Currently, these aforementioned problems can be handled by certain post-build thermal treatments that are generally performed in a hot isostatic pressing (HIP) facility under high pressure, or via rapid annealing, to restrain segregation and the generation of pores and cracks [31,32]. Therefore, HIP is a prevalent thermomechanical treatment that enables the decrease and elimination of inherent defects in as-printed parts manufactured via PBF technology [33]. This result mainly relies on decreasing the number of cracks initially shuttling within the products. As opposed to HIP, thermal annealing is well-known because it can further optimize nanocrystalline grain size and other such properties of printed HEAs [34]. Recently, anumber of investigations on PBF-printed HEAs have been carried out to achieve high-performance HEAs; for example, the influence of processing parameters and annealing treatments on the microstructure and tensile properties of PBF-printed CoCrFeNiMn were studied to obtain the perfect combination of high strength and high ductility [35]. Li et al., researched the correlation between formation parameters and HIP on microstructure and tensile properties [36], but there has been little research on the hydrogen embrittlement susceptibility of such HEAs. During the service or processing of HEAs in hydrogen-containing environments, hydrogen atoms will be absorbed on the surface and then further diffused and gathered in certain positions within the alloy, generating hydrogen partial pressure, accelerating the movement of dislocation; reducing the cohesion between grain boundaries, resulting in a decline in strength and plasticity; and inducing hydrogen-induced cracking. When massive CoCrFeNiMn HEAs are formed using PBF printing in a hydrogen medium for a long period of time and are subjected to external forces, hydrogen-induced microcracks will occur in the CoCrFeNiMn HEAs and gradually expand, and then brittle fracture will occur, leading to the premature failure of the material. Additionally, HE fracture is usually uncertain and sudden, which often leads to serious failure accidents. At present, there is no unified explanation for the hydrogen embrittlement fracture mechanism of CoCrFeNiMn HEAs made using PBF. However, the study of the HE mechanism is of great significance for the protection against HE and the development of anti-hydrogen embrittlement HEAs.

In view of this issue, this work mainly studies HE sensitivity, the HE fracture mechanism of CoCrFeNiMn HEA 3D-printed parts, and the influence of post-treatment technology (annealing and hot isostatic pressing) on the hydrogen embrittlement behavior of CoCrFeNiMn HEAs formed via PBF printing. To do so, the effect of post-thermal treatment, including HIP and annealing, on microstructure, residual stress, and the hydrogen

brittleness resistance of as-built CoCrFeNiMn HEAs formed via PBF is investigated using microscopic characterization analysis and in situ electrochemical hydrogen-charging slow strain rate stretching. In addition, the corresponding deformation and fracture mechanisms are discussed.

2. Experimental Procedure

2.1. Material

This work focuses on vacuum gas-atomized CoCrFeMnNi HEA powders (provided by Jiangsu Willari New Material Technology Co. Ltd., Jiangsu, China), whose sizes are located in the 10–50 μm range, meeting the conditions for PBF and HIP processing as well as for the annealing material. The chemical composition and physical properties of the HEA powders in different conditions are given in Table 1.

Table 1. Chemical composition and physical properties of five different elements of CoCrFeMnNi HEA powders.

Elements	Crystal Structure	Atomic Radius (nm)	Melting Point (°C)	Chemical Composition (wt%)
Co	HCP	0.130	1495	20.25
Cr	BCC	0.125	1860	19.12
Fe	BCC	0.125	1540	20.21
Mn	FCC	0.130	1250	19.77
Ni	FCC	0.130	1450	20.65

2.2. Processing

2.2.1. Powder-Bed Fusion (PBF)

PBF printing with HEA powder was performed using an EP-M250 printer equipped with a continuous ytterbium fiber laser (wavelength: 1060–1090 nm) and an F-θ lens system. Before printing, the powder was vacuum-dried and kept at 90 °C for 2 h to remove moisture to ensure adequate dryness of the powder. We selected 316L stainless steel with a similar chemical composition to CoCrFeNiMn HEA as the formation substrate. In the printing process, the laser scanning strategy adopts a layer rotation of 67° (as shown in Figure 1) so that it can effectively reduce the stress concentrated inside the sample and minimize faults and macroscopic cracks. To avoid the problem of powder oxidation during the formation process, high-purity argon (99.999%) was selected as the protective gas, and the oxygen content was controlled below 100 ppm. By optimizing a series of processes and parameters, bulk energy density was calculated at 100 J/mm^3. Under this condition, CoCrFeNiMn HEA with comprehensive mechanical properties such as 13.8% elongation, 587.5 MPa yield strength, and 666.3 MPa tensile strength were printed. Compared with the as-cast and welded CoCrFeNiMn HEA, the tensile strength of the PBF-printed samples showed significant improvement.

2.2.2. Annealing and Hot Isostatic Pressing (HIP)

In this experiment, annealing and HIP were applied to further improve the properties of the printed samples. (1) Annealing process: the printed samples were sintered at 900 °C in an SG-XL1200 high-temperature box furnace for 1 h and then immediately cooled to room temperature. (2) HIP process: the printed samples were placed in an HIP QIH-9 from Quintus Technologies AB (Avure Technologies, Inc., Västerås, Sweden), which was equipped with a molybdenum heating system, heated to 1150 °C within 2 h, and then preserved for 3 h at the high pressure of 150 MPa under a high-purity argon protection atmosphere. The state of the sample after PBF printing is defined as S1. The state after PBF + annealing is defined as S2. The state after PBF + HIP is defined as S3.

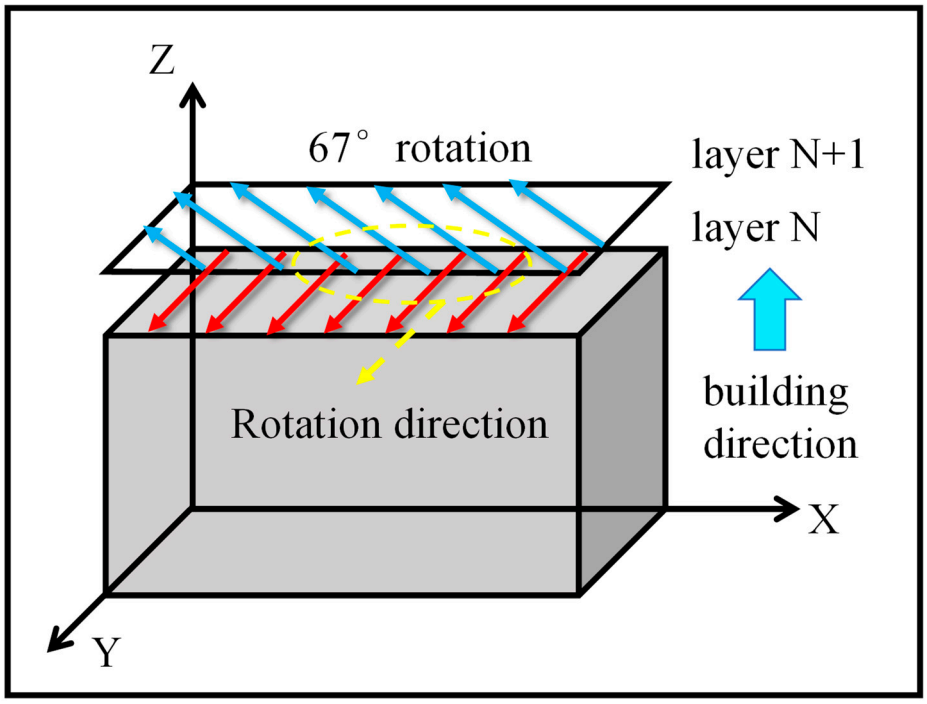

Figure 1. PBF forming diagram and path planning.

2.3. Measurement and Characterization

2.3.1. Basic Physical Details Measurements

The block of CoCrFeNiMn HEA samples printed using PBF were etched in aqua regia solution for 15–30 s after standard metallographic preparation. A Zeiss optical microscope (ZEISS Axio Lab.A1, ZEISS Industrial Metrology, Germany) was used to observe the microstructure of different surfaces. The tensile properties of the specimens were tested at room temperature (293 K) and at liquid nitrogen low temperature (77 K) at a tensile rate of 1 mm/min on a slow strain rate tensile testing machine (Liangong Testing, Jinan, China). Residual stress of the as-built HEAs was measured using an XRD (X-350A, Dandong HaoyuanChina) ($\sin^2\omega$ method). The X-ray beam diameter was approximately 2 mm. The X-ray source was Cr-Kα X-ray, and the diffraction plane was (111). In the stress calculation, Poisson's ratio was set to 0.5. The speed for ladder scanning was 0.05 deg s^{-1}, and the time constant was 1 s. The tube voltage and current were 20 kV and 5 mA, respectively. The scanning angle of 2 h was in the range of 76 to 84°. Residual stress determination using the XRD method indicated average stresses in the volume of HEAs defined by the irradiated area. The penetration depth of the Cr-Kα X-ray beam was about 5.5. The heeling angle was set to be close to zero degrees. The hardness distribution was determined using the Vickers hardness tester (model: DHV-1000ZTEST, Shidai ShanFeng, Beijing, China), and the test parameter was set at 1 kgf (loading) and maintained for 15 s. Ten different areas on the surface of the sample were randomly selected for testing. The maximum and minimum values were removed, and the average hardness value of the remaining 8 locations was calculated as the final Vickers hardness value (HV).

2.3.2. In Situ Electrochemical Hydrogen-Charging Slow Strain Rate Tensile Test

During the loading process of the sample subjected to tensile force, the DC power supply was synchronously turned on to apply cathode potential until the sample fractured, and the state of hydrogen-charging was maintained through the entire process of tensile force. Meanwhile, during this process, the strain rate was set as 10^{-5} s^{-1}, an electric current density of 15 mA/cm^2 was selected, and the hydrogen filling solution ratio was 0.5 mol/L H_2SO_4 + 2 g/L CH_4N_2S.

3. Results and Discussion

Figure 2 shows the macroscopic surface morphology of the tensile-fracture side of the PBF-printed CoCrFeNiMn HEA without hydrogen-charging (in air) and in a hydrogen-charging solution. The lateral surface of the sample without hydrogen-charging shows obvious necking of the alloy (Figure 2(a1)), and the shear lip feature was also observed, indicating that the fracture mechanism includes a ductile fracture [37]. In contrast, no obvious deformation or necking phenomena were observed in the sample after hydrogen-charging (Figure 2(b1)), but multiple cracks expanded at the same time, indicating that brittle fracture occurred. As shown in Figure 2(c1), many secondary cracks perpendicular to the direction of tensile stress were generated in the sample, and many crack branches appeared during propagation.

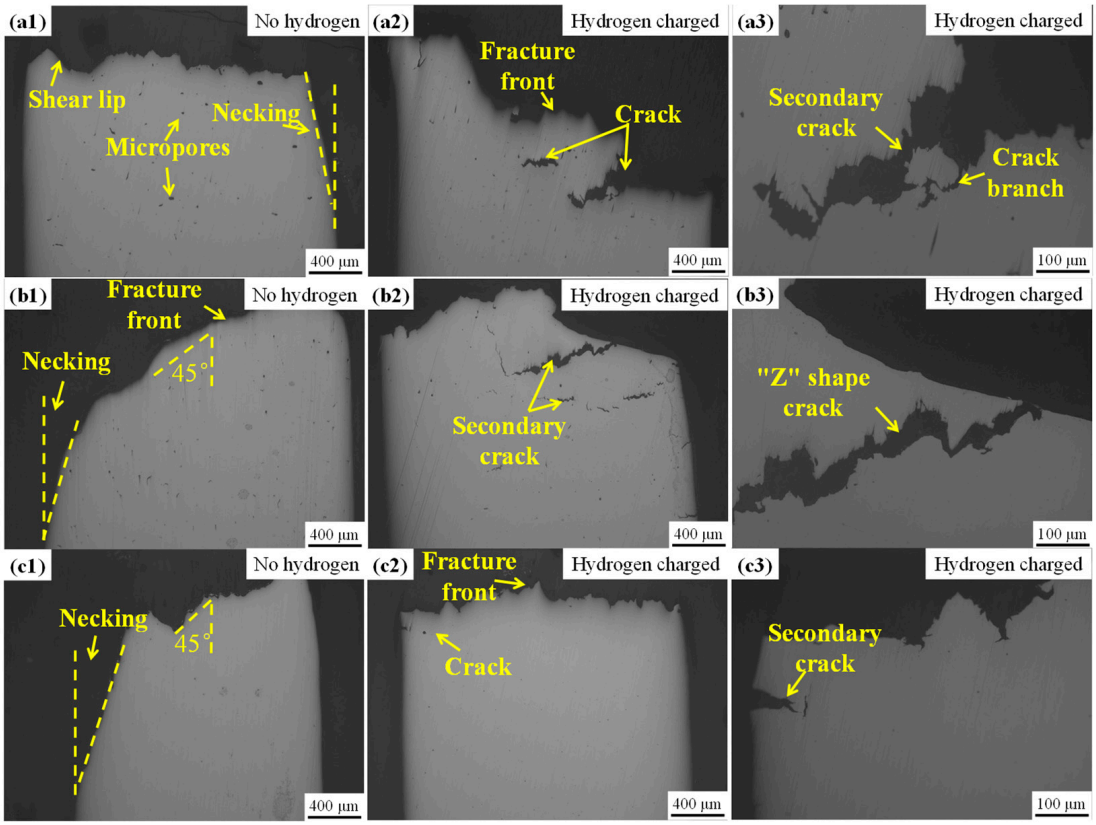

Figure 2. Macro morphology of the tensile-fracture side surface of CoCrFeNiMn HEA samples in three different states: (**a1**–**a3**) S1 state; (**b1**–**b3**) S2 state; (**c1**–**c3**) S3 state, and (**a1**,**b1**,**c1**) without hydrogen (in air); (**a2**,**b2**,**c2**) in hydrogen-filled solution; (**a3**,**b3**,**c3**) secondary cracks and branches (local enlarged view).

The surface morphology of the tensile-fracture side of the sample annealed at 900 °C is shown in Figure 2(b1–b3). The edge of the sample without hydrogen-charging shows an obvious necking phenomenon, which is more obvious than that of the PBF-printed sample, indicating an improvement in plasticity. In addition, the fracture front presents a 45° shear fracture, indicating a plastic fracture. In a state of dynamic electrochemical hydrogen-charging, many secondary cracks appear on the surface of the fracture side, which shows a "Z" shape expansion; simultaneously, small crack branches are generated. There is no obvious shrinkage at the edge of the side surface under the condition of hydrogen-charging, indicating that the fracture mode of the annealed sample under the condition of hydrogen-charging is one of brittle fracture.

The surface morphology of the sample on the fracture side in air and in a hydrogen-filled solution after HIP is shown in Figure 2(c1–c3). The necking phenomenon is observed

on the surface of the fractured side without hydrogen-charging, and the characteristic of a 45° shear fracture is also observed. Compared with the PBF-printed and annealed samples, the necking degree of the fractured side surface is more significant in air, and the quantity of micropores and microcracks also decreases, showing the highest plasticity of samples in these three states. Meanwhile, in the electrochemical hydrogen-charging environment, the surface of the fracture side shows that the fracture front is relatively flat, and the necking phenomenon of both side edges is not obvious, indicating a brittle fracture mode. In addition, the number of secondary cracks on the surface of the fracture side obviously decreases after HIP treatment.

The secondary surface cracks are caused by the fact that the alloy acts as a cathode, and the hydrogen atom activity on the surface is relatively high during the process of electrochemical hydrogen-charging, which damages the surface of the PBF-printed CoCrFeNiMn HEA and causes surface cracks under the function of tensile stress [38]. The number of surface cracks decreases after HIP, which indicates that the sample is less damaged caused by hydrogen and that its hydrogen brittleness resistance is enhanced after HIP.

The tensile-fracture morphology of PBF-printed CoCrFeNiMn HEA in a hydrogen-filled solution was analyzed and observed via scanning electron microscopy, as shown in Figure 3(a1). Compared with the fracture morphology in air, we found that the fracture characteristics of the PBF-printed sample under a hydrogen-charging condition mainly constituted brittle fracture. There were many cross-tearing edges, stepped morphology, and cleavage planes on the fracture surface (Figure 3(a2)), which are typical brittle fracture modes. At high magnification, dimples were observed (Figure 3(a3)), which occupied a small area, indicating the presence of ductile fracture.

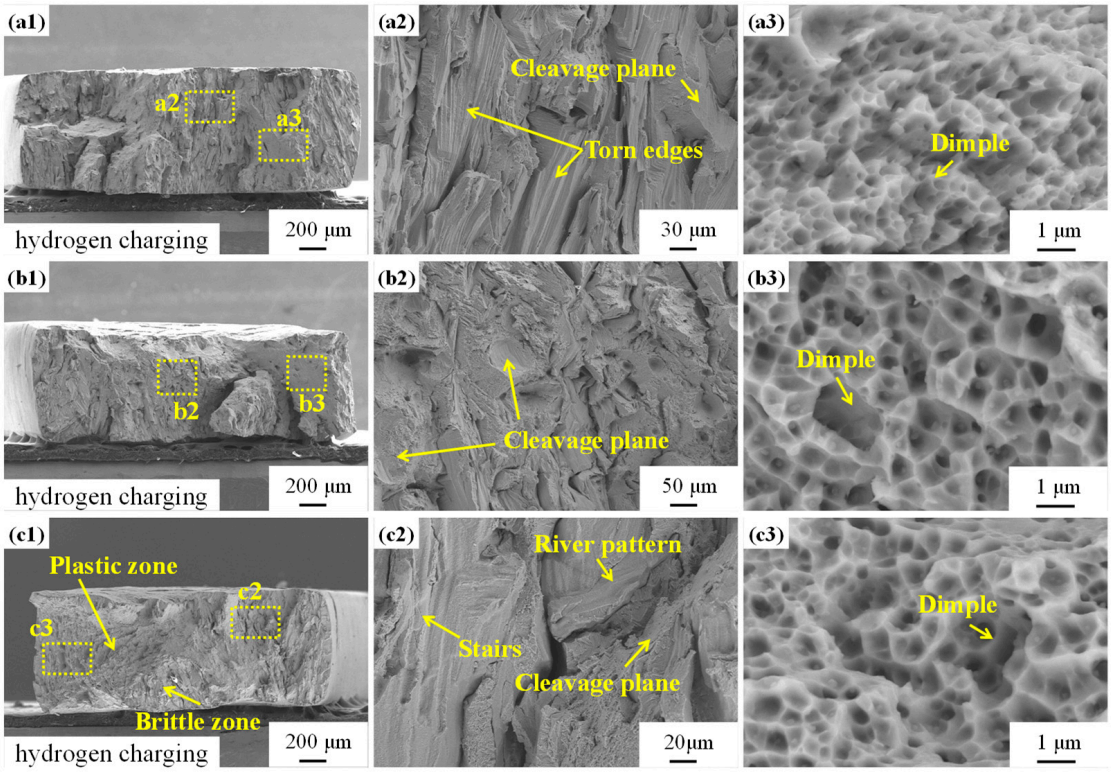

Figure 3. Tensile-fracture morphology of CoCrFeNiMn HEA samples in three different states in a hydrogen-filled solution: (**a1**–**a3**) S1 state; (**b1**–**b3**) S2 state; (**c1**–**c3**) S3 state.

The sample in the S2 state still shows obvious brittle fracture in the hydrogen-charging environment, with cleavage planes and river patterns as fracture features (Figure 3(b2)). In addition, the dimple area is larger than that of the PBF-printed sample, and the high-magnification image shows that the dimple size is larger and deeper, indicating that the

plasticity has been improved, which is consistent with the results of the tensile stress–strain curve in the hydrogen-charged environment.

After HIP at 115 °C, the fracture of the sample shows obvious partitions, including a brittle zone and a plastic zone (Figure 3(c1)). The characteristics of brittle fracture appear at the edge of the fracture, which may be caused by the high concentration of hydrogen on the alloy surface due to dynamic electrochemical hydrogen-charging and the inherent defects on the sample surface, which result in the existence of a high stress intensity factor on the sample surface [38]. Stepped features, river patterns, and cleavage planes still exist on the fracture surface (Figure 3(c2)), indicating that it is brittle fracture. However, the plastic zone area increased, and there are evenly distributed dimples presenting large and deep characteristics (Figure 3(c3)). Accordingly, its plasticity has been further improved. In general, larger and deeper dimple distribution indicates better ductility [39].

The above cracks relate to the measured residual stresses shown in Figure 4, in which the residual stresses were 338 ± 4 MPa, 105 ± 4 MPa, and 44 ± 4 MPa for the samples in the S1, S2, and S3 states, respectively. The residual stress for all samples was tensile stress, resulting in the observable surface crack in Figure 2. It can be calculated that residual stress decreased 68.9% and 86.9% from the S1 to the S2 and S3 states, respectively. The cracks produced by residual stress were mainly crystal cracks, which resulted from hot cracks because the liquid film formed by a low eutectic melting point (residual liquid) weakened the bond between the grains and generated a crack under the function of residual stress [40]. Consequently, the greater the tensile stress was, the greater the generated crack widths became.

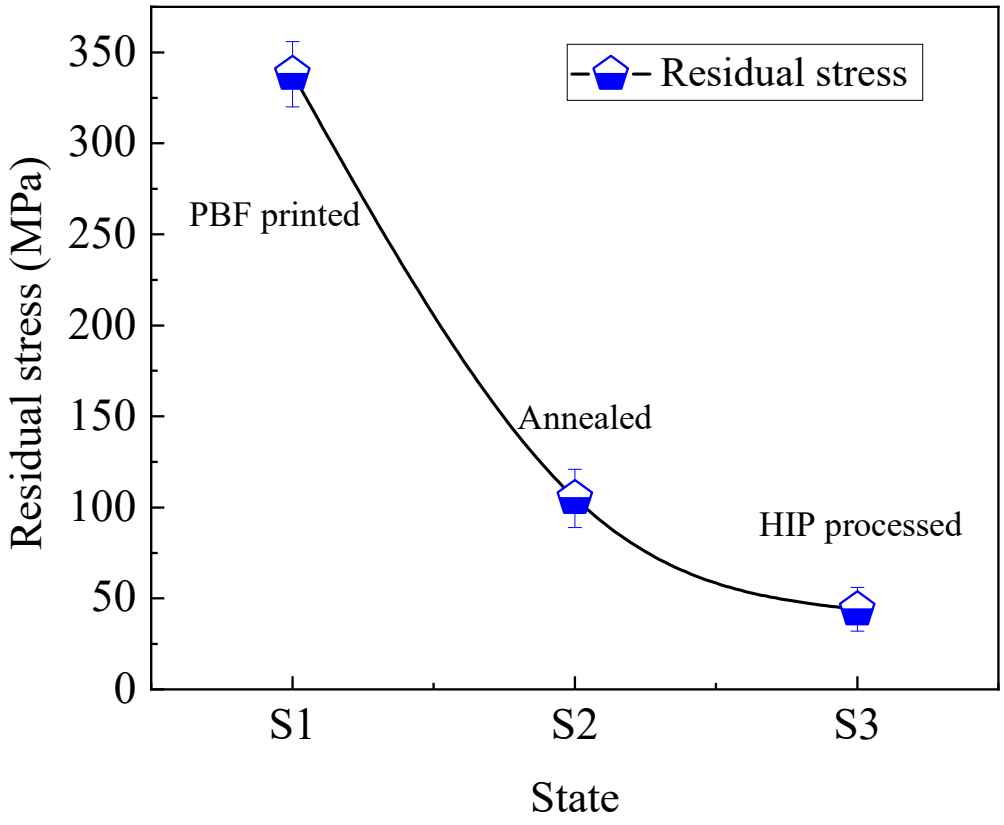

Figure 4. The distribution of residual stress values of SLM printed CoCrFeNiMn HEA in three states.

Figure 5 shows the distribution of the hardness values of PBF-printed CoCrFeNiMn HEA in the three states. Annealing and HIP have important effects on hardness, which shows a decreasing trend correlating with temperature increases. Specifically, the hardness value of the SLM printed sample was 211.2 ± 2 HV and 197.6 ± 2 HV for the annealed sample and 194.1 ± 2 HV for the HIP sample. This general behavior can be attributed

to microstructural changes, especially the coarsening and coalescence of metal particles caused by temperature increases. These changes can be seen to relate to the effect of high temperature and annealing effects activating coarsening and coalescing mechanisms.

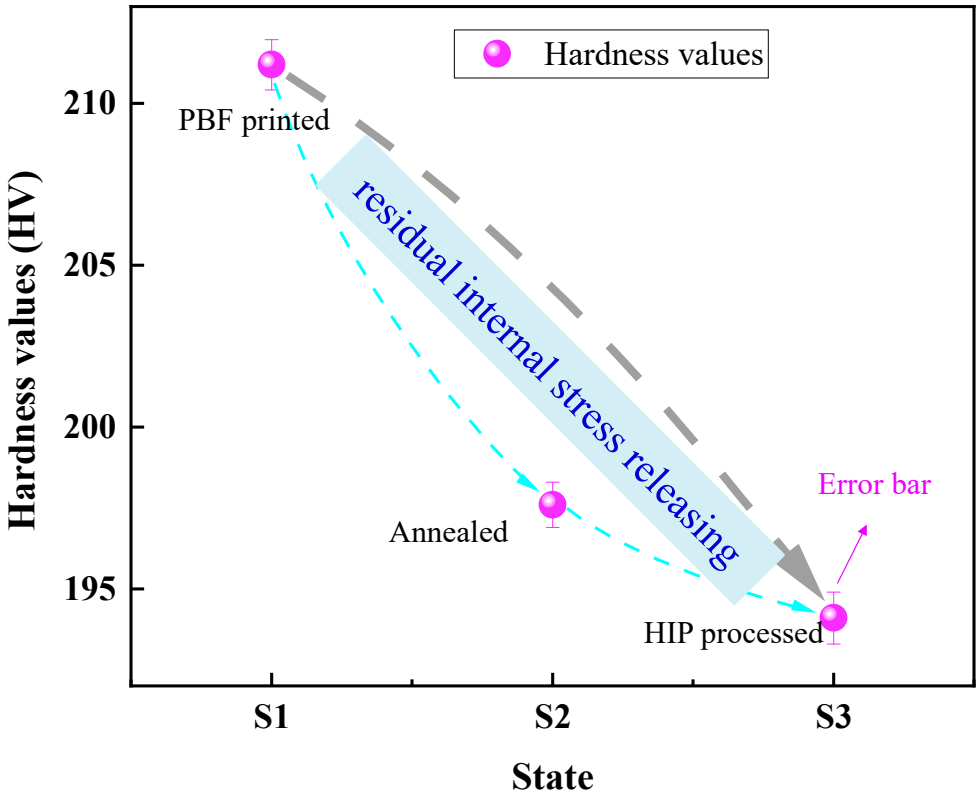

Figure 5. Hardness of CoCrFeNiMn HEA samples in three different states.

Figure 6 shows the slow strain rate tensile results of the samples in three different states without hydrogen-charging (in air) and under hydrogen-charging conditions. The HE sensitivity index of the samples in three different states after hydrogen-charging was calculated according to Formulas (2) and (3), and their strength and plastic loss rate were obtained (Figure 6b). As can be seen from the engineering stress–strain curve (Figure 6a), it is obvious that the presence of a hydrogen atom has a negative effect on the strength and plasticity of the alloy, and the hydrogen brittleness resistance of the sample after annealing and HIP can be significantly improved. The slope of the engineering stress–strain curve in an elastic stage is almost the same in air and in a hydrogen environment, indicating that hydrogen filling does not affect the elastic deformation stage of materials.

The sensitivity of HE was evaluated using plastic loss rate (δ_{HE}) and strength loss rate (UTS_{HE}). The higher the loss rate, the higher the sensitivity of HE [41]. The calculation formula of loss rate is as follows:

$$\delta_{HE}(\%) = \frac{\delta_0 - \delta_H}{\delta_0} \times 100\% \quad (1)$$

where δ_0 and δ_H represent the growth rate of the interrupted sample in air and in a hydrogen-charging environment, respectively.

$$UTS_{HE}(\%) = \frac{UTS_0 - UTS_H}{UTS_0} \times 100\% \quad (2)$$

where UTS_{HE}, UTS_0, and UTS_H denote strength loss rate, the tensile strength of the sample in air, and that in a hydrogen-charging environment, respectively.

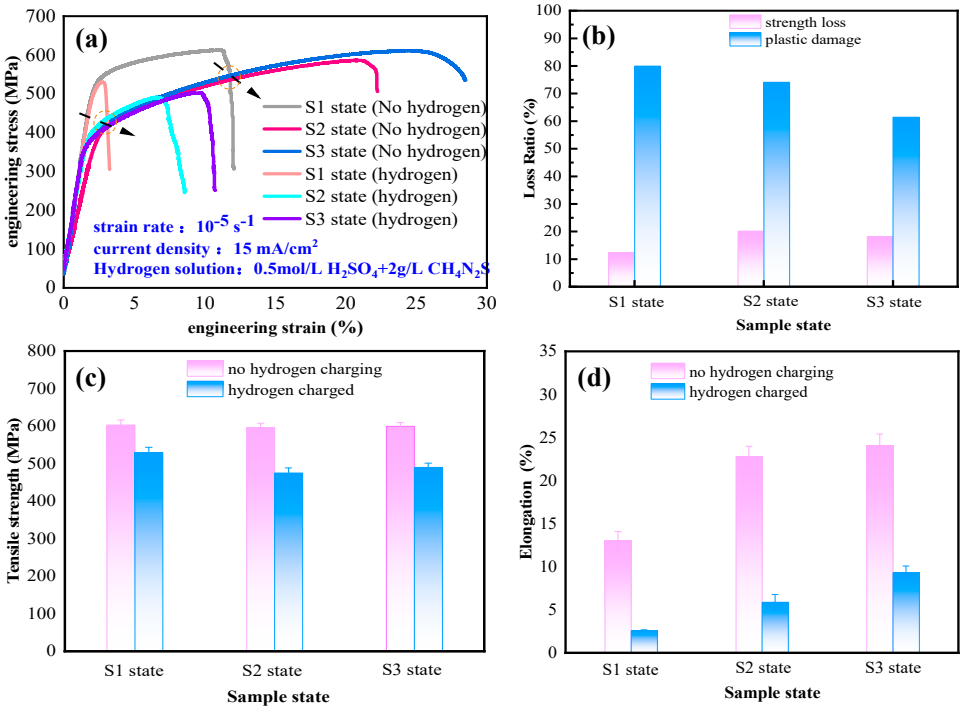

Figure 6. Dynamic electrochemical hydrogen-charging slow strain rate tensile results of CoCrFeNiMn HEA: (**a**) typical engineering stress–strain curve; (**b**) strength and plastic loss rate; (**c**) tensile strength; (**d**) elongation.

Under the conditions of a hydrogen-charging solution (0.5 mol/L H_2SO_4 + 2 g/L CH_4N_2S) and current density of 15 mA/cm^2, the strength loss rate of samples in a printed state is 12.3%, and the plastic loss rate is 80%. After annealing, the strength loss rate is 20.2%, and the plastic loss rate is 74.12%. After HIP, the strength loss rate is 18.2%, and the plastic loss rate is 61.4%. The results show that the introduction of a hydrogen atom has a negative effect on tensile strength and elongation after fracture. In addition, samples in both the S1 and S2 states show high HE sensitivity and suffer serious hydrogen damage. However, the plastic loss rate of PBF-printed samples after HIP treatment is significantly improved (23.2%). This indicates the lower HE sensitivity and higher HE resistance of PBF-printed parts after HIP treatment. In air (without hydrogen-charging), the tensile strength of the printed PBF samples in the three states remains at about 600 MPa. However, the elongation after fracture is significantly increased to 13% in the S1 state, to 22.8% (a 75.4% improvement) in the S2 state, and to 24.1% (an 85.4% improvement) in the HIP state. With the increase in temperature and the intervention of pressure, the hydrogen brittleness resistance of PBF-printed samples can be significantly improved, which may be due to the change in microstructure and the reduction of pores and gaps [36].

Based on the above results and analysis, the conclusion can be drawn that two hydrogen-induced cracking mechanisms, including adsorption-induced dislocation emission (AIDE) and hydrogen-enhanced local ductility (HELD), cooperate in this work. According to the former mechanism, hydrogen atoms will be adsorbed on the metal surface due to the high hydrogen concentration on the outer surface of the alloy, resulting in the initiation of hydrogen-induced cracks, while the latter mechanism shows that the local rich assembly of hydrogen atoms in metal accelerates dislocation motion and plastic deformation, resulting in the local plastic deformation of fracture characteristics and macroscopic brittle fracture [38]. In the in situ electrochemical hydrogen-charging slow strain rate tensile test, there is a high hydrogen concentration on the surface of the alloy, and the electrochemical hydrogen-charging time is longer. In addition, hydrogen atoms have a high solubility rate in the CoCrFeNiMn HEA [42], so more hydrogen atoms can be dissolved inside the sample. Based on this, this paper can assume the synergistic effect of the two mechanisms.

In the process of in situ electrochemical hydrogen-charging, most hydrogen atoms accumulate on the subsurface of the sample [43]. For the CoCrFeNiMn HEA formed using PBF printing, the inherent characteristics (extremely fast heating and cooling rates) lead to the introduction of an extremely high dislocation density, which has the function of transporting hydrogen atoms and becomes a channel for hydrogen enrichment and rapid diffusion during the stretching process [44]. At the same time, a high dislocation density and a corresponding high local residual strain further increases the concentration of hydrogen atoms at the grain boundary. Defects such as grain boundaries, dislocation, and associated strain field, as well as micro-holes inevitably generated using SLM printing, are typical hydrogen diffusion trap locations that have a poor bonding force with hydrogen atoms [45], resulting in the alloy having high HE sensitivity. With the loading of tensile stress, the sample is in a plane strain state, and the diffusion and enrichment of hydrogen atoms in the hydrogen trap are strengthened. When the local hydrogen concentration and stress are high enough, hydrogen embrittlement cracks will begin to initiate and grow t. On the other hand, hydrogen atoms easily accumulate at the crack tip, and solid dissolved hydrogen atoms in the matrix can aggravate dislocation motion. Therefore, local plastic deformation occurs easily near the crack tip, resulting in the generation of micropores or holes. The aggregation and merging of these micropores will further grow and expand the crack and eventually lead to the fracture of the sample.

For the samples annealed at 900 °C, the local residual strain is released, the dislocation density is reduced, and the number of hydrogen traps is reduced, resulting in the annealed sample retaining a lower sensitivity to hydrogen embrittlement. For the samples after hot isostatic pressing at 1150 °C, the further increase in annealing temperature and the interaction of high-pressure gas make the local residual strain release more complete, and the dislocation density decreases substantially. Meanwhile, the density of the samples (such as the closure of micropores and microcracks) is also improved, thus reducing the number of hydrogen traps. This can effectively prevent the infiltration of hydrogen so that the hydrogen diffusion channel is eliminated as much as possible and the hydrogen embrittlement sensitivity is lowest. Accordingly, the samples treated using hot isostatic pressing showed the best hydrogen embrittlement fracture resistance.

4. Conclusions

In this paper, the effects of post-treatment processes, including annealing and HIP, on the microstructure, residual stress, mechanical properties, and resistance to hydrogen embrittlement behavior of PBF-printed CoCrFeNiMn HEAs were studied. The post-treatment results demonstrated a decrease in dislocation density due to the release of residual stress (338 MPa, 105 MPa, and 44 MPa in three states), which is the key to the decrease in hardness (211.2 HV of printed samples, 197.6 HV of annealed samples, and 194.1 HV of HIP samples). Finally, research on room- and low-temperature hydrogen embrittlement characteristics showed that after post-treatment (annealing and HIP), resistance to hydrogen embrittlement is improved. These excellent behaviors could provide some useful solutions for enhanced mechanical properties and the anti-hydrogen embrittlement ability of PBF-printed HEAs and other similar products.

Author Contributions: Conceptualization, S.F., Z.A. and B.Y.; methodology, S.F. and J.H.; software, J.H.; validation, B.Y.; formal analysis, B.Y.; investigation, B.Y.; resources, G.G.; data curation, L.H.; writing—original draft preparation, S.F.; writing—review and editing, Z.A.; visualization, L.H.; supervision, Z.A.; project administration, Z.A.; funding acquisition, 2020 Chengdu City International Cooperation Funding Program (No. 2020-GH02-00058-HZ). All authors have read and agreed to the published version of the manuscript.

Funding: 2020 Chengdu City International Cooperation Funding Program (No. 2020-GH02-00058-HZ).

Data Availability Statement: All relevant data are within the paper.

Acknowledgments: The authors acknowledge the financial support from 2020 Chengdu City International Cooperation Funding Program (No. 2020-GH02-00058-HZ).

Conflicts of Interest: The authors declare that they have no known competing financial interests or personal relationships that could have appeared to influence the work reported in this paper.

References

1. Kenel, C.; Casati, N.P.M.; Dunand, D.C. 3D ink-extrusion additive manufacturing of CoCrFeNi high-entropy alloy micro-lattices. *Nat. Commun.* **2019**, *10*, 904. [CrossRef] [PubMed]
2. Gorsse, S.; Hutchinson, C.; Gouné, M.; Banerjee, R. Additive manufacturing of metals: A brief review of the characteristic microstructures and properties of steels, Ti-6Al-4V and high-entropy alloys. *Sci. Technol. Adv. Mater.* **2017**, *18*, 584–610. [CrossRef] [PubMed]
3. Li, X. Additive Manufacturing of Advanced Multi-Component Alloys: Bulk Metallic Glasses and High Entropy Alloys. *Adv. Eng. Mater.* **2018**, *20*, 1700874. [CrossRef]
4. Miracle, D.B.; Senkov, O.N. A critical review of high entropy alloys and related concepts. *Acta Mater.* **2017**, *122*, 448–511. [CrossRef]
5. Han, C.; Fang, Q.; Shi, Y.; Tor, S.B.; Chua, C.K.; Zhou, K. Recent Advances on High-Entropy Alloys for 3D Printing. *Adv. Mater.* **2020**, *32*, e1903855. [CrossRef] [PubMed]
6. Bricín, D.; Véle, F.; Jansa, Z.; Špirit, Z.; Kotous, J.; Kubátová, D. The structure and the properties of WC-Co samples produced by SLM technology and carbon-doped prior to HIP processing. *Rapid Prototyp. J.* **2022**, *28*, 102–122. [CrossRef]
7. Olakanmi, E.O.T.; Cochrane, R.F.; Dalgarno, K.W. A review on selective laser sintering/melting (SLS/SLM) of aluminium alloy powders: Processing, microstructure, and properties. *Prog. Mater. Sci.* **2015**, *74*, 401–477. [CrossRef]
8. Gu, D.D.; Meiners, W.; Wissenbach, K.; Poprawe, R. Laser additive manufacturing of metallic components: Materials, processes and mechanisms. *Int. Mater. Rev.* **2012**, *57*, 133–164. [CrossRef]
9. Tarakçı, G.; Khan, H.M.; Yılmaz, M.S.; Özer, G. Effect of building orientations and heat treatments on AlSi10Mg alloy fabricated by selective laser melting: Microstructure evolution, mechanical properties, fracture mechanism and corrosion behavior. *Rapid Prototyp. J.* **2022**, *28*, 1609–1621. [CrossRef]
10. Wang, D.; Wei, X.; Liu, J.; Xiao, Y.; Yang, Y.; Liu, L.; Tan, C.; Yang, X.; Han, C. Lightweight design of an AlSi10Mg aviation control stick additively manufactured by laser powder bed fusion. *Rapid Prototyp. J.* **2022**, *28*, 1869–1881. [CrossRef]
11. Khorasani, M.; Ghasemi, A.; Leary, M.; Sharabian, E.; Cordova, L.; Gibson, I.; Downing, D.; Bateman, S.; Brandt, M.; Rolfe, B. The effect of absorption ratio on meltpool features in laser-based powder bed fusion of IN718. *Opt. Laser Technol.* **2022**, *153*, 108263. [CrossRef]
12. Yap, C.Y.; Chua, C.K.; Dong, Z.L.; Liu, Z.H.; Zhang, D.Q.; Loh, L.E.; Sing, S.L. Review of selective laser melting: Materials and applications. *Appl. Phys. Rev.* **2015**, *2*, 041101. [CrossRef]
13. Chen, H.; Gu, D.; Xiong, J.; Xia, M. Improving additive manufacturing processability of hard-to-process overhanging structure by selective laser melting. *J. Mater. Process. Technol.* **2017**, *250*, 99–108. [CrossRef]
14. Lu, Z.; Wang, H.; Chen, M.; Baker, I.; Yeh, J.; Liu, C.; Nieh, T. An assessment on the future development of high-entropy alloys: Summary from a recent workshop. *Intermetallics* **2015**, *66*, 67–76. [CrossRef]
15. Shafeie, S.; Guo, S.; Erhart, P.; Hu, Q.; Palmqvist, A. Balancing Scattering Channels: A Panoscopic Approach toward Zero Temperature Coefficient of Resistance Using High-Entropy Alloys. *Adv. Mater.* **2019**, *31*, e1805392. [CrossRef] [PubMed]
16. Praveen, S.; Kim, H.S. High-Entropy Alloys: Potential Candidates for High-Temperature Applications—An Overview. *Adv. Eng. Mater.* **2018**, *20*, 1700645. [CrossRef]
17. Li, Z.; Pradeep, K.G.; Deng, Y.; Raabe, D.; Tasan, C.C. Metastable high-entropy dual-phase alloys overcome the strength–ductility trade-off. *Nature* **2016**, *534*, 227–230. [CrossRef]
18. Ye, Y.; Wang, Q.; Lu, J.; Liu, C.; Yang, Y. High-entropy alloy: Challenges and prospects. *Mater. Today* **2015**, *19*, 349–362. [CrossRef]
19. Gludovatz, B.; Hohenwarter, A.; Catoor, D.; Chang, E.H.; George, E.P.; Ritchie, R.O. A fracture-resistant high-entropy alloy for cryogenic applications. *Science* **2014**, *345*, 1153–1158. [CrossRef]
20. Zhao, S.; He, L.-X.; Fan, X.-X.; Liu, C.-H.; Long, J.-P.; Wang, L.; Chang, H.; Wang, J.; Zhang, W. Microstructure and chloride corrosion property of nanocrystalline AlTiCrNiTa high entropy alloy coating on X80 pipeline steel. *Surf. Coat. Technol.* **2019**, *375*, 215–220. [CrossRef]
21. Zhao, B.; Zhu, M.; Yuan, Y.; Guo, S.; Yin, S. Comparison of Corrosion Resistance of CoCrFeMnNi High Entropy Alloys with Pipeline Steels in an Artificial Alkaline Soil Solution. *J. Chin. Soc. Corros. Prot.* 2022. [CrossRef]
22. An, T.; Peng, H.; Bai, P.; Zheng, S.; Wen, X.; Zhang, L. Influence of hydrogen pressure on fatigue properties of X80 pipeline steel. *Int. J. Hydrog. Energy* **2017**, *42*, 15669–15678. [CrossRef]
23. Yokoyama, K.; Eguchi, T.; Asaoka, K.; Nagumo, M. Effect of constituent phase of Ni–Ti shape memory alloy on susceptibility to hydrogen embrittlement. *Mater. Sci. Eng. A* **2004**, *374*, 177–183. [CrossRef]
24. Marchi, C.S.; Somerday, B.; Robinson, S. Permeability, solubility and diffusivity of hydrogen isotopes in stainless steels at high gas pressures. *Int. J. Hydrog. Energy* **2007**, *32*, 100–116. [CrossRef]
25. Pu, Z.; Chen, Y.; Dai, L. Strong resistance to hydrogen embrittlement of high-entropy alloy. *Mater. Sci. Eng. A* **2018**, *736*, 156–166. [CrossRef]
26. Zhao, S.; Li, S.; Hou, W.; Hao, Y.; Yang, R.; Misra, R. The influence of cell morphology on the compressive fatigue behavior of Ti-6Al-4V meshes fabricated by electron beam melting. *J. Mech. Behav. Biomed. Mater.* **2016**, *59*, 251–264. [CrossRef]

27. Liu, Y.; Li, S.; Wang, H.; Hou, W.; Hao, Y.; Yang, R.; Sercombe, T.; Zhang, L. Microstructure, defects and mechanical behavior of beta-type titanium porous structures manufactured by electron beam melting and selective laser melting. *Acta Mater.* **2016**, *113*, 56–67. [CrossRef]
28. Kwon, Y.J.; Won, J.W.; Park, S.H.; Lee, J.H.; Lim, K.R.; Na, Y.S.; Lee, C.S. Ultrahigh-strength CoCrFeMnNi high-entropy alloy wire rod with excellent resistance to hydrogen embrittlement. *Mater. Sci. Eng. A* **2018**, *732*, 105–111. [CrossRef]
29. Nygren, K.E.; Wang, S.; Bertsch, K.; Bei, H.; Nagao, A.; Robertson, I.M. Hydrogen embrittlement of the equi-molar FeNiCoCr alloy. *Acta Mater.* **2018**, *157*, 218–227. [CrossRef]
30. Koyama, M.; Ichii, K.; Tsuzaki, K. Grain refinement effect on hydrogen embrittlement resistance of an equiatomic CoCrFeMnNi high-entropy alloy. *Int. J. Hydrog. Energy* **2019**, *44*, 17163–17167. [CrossRef]
31. Ruttert, B.; Ramsperger, M.; Roncery, L.M.; Lopez-Galilea, I.; Körner, C.; Theisen, W. Impact of hot isostatic pressing on microstructures of CMSX-4 Ni-base superalloy fabricated by selective electron beam melting. *Mater. Des.* **2016**, *110*, 720–727. [CrossRef]
32. Ramsperger, M.; Roncery, L.M.; Lopez-Galilea, I.; Singer, R.F.; Theisen, W.; Körner, C. Solution Heat Treatment of the Single Crystal Nickel-Base Superalloy CMSX-4 Fabricated by Selective Electron Beam Melting. *Adv. Eng. Mater.* **2015**, *17*, 1486–1493. [CrossRef]
33. Kondo, D.; Yasuda, H.; Nakano, T.; Cho, K.; Ikeda, A.; Ueda, M.; Nagamachi, Y. The Effect of HIP Treatment on the Mechanical Properties of Titanium Aluminide Additive Manufactured by EBM. In Proceedings of the 12th International Conference on Hot Isostatic Pressing (HIP'17), Sydney, Australia, 5–8 December 2017.
34. La, P.; Wei, Y.; Yang, Y.; Bai, Y.; Lu, X.; Guo, X.; Wang, H. Effect of annealing on microstructure and mechanical properties of bulk nanocrystalline Fe3Al alloy with 5wt.% Cu prepared by aluminothermic reaction. *Mater. Sci. Eng. A* **2011**, *528*, 7140–7148. [CrossRef]
35. Zhu, Z.; Nguyen, Q.; Ng, F.; An, X.; Liao, X.; Liaw, P.; Nai, S.; Wei, J. Hierarchical microstructure and strengthening mechanisms of a CoCrFeNiMn high entropy alloy additively manufactured by selective laser melting. *Scr. Mater.* **2018**, *154*, 20–24. [CrossRef]
36. Li, R.; Niu, P.; Yuan, T.; Cao, P.; Chen, C.; Zhou, K. Selective laser melting of an equiatomic CoCrFeMnNi high-entropy alloy: Processability, non-equilibrium microstructure and mechanical property. *J. Alloys Compd.* **2018**, *746*, 125–134. [CrossRef]
37. Tong, Z.; Ren, X.; Jiao, J.; Zhou, W.; Ren, Y.; Ye, Y.; Larson, E.A.; Gu, J. Laser additive manufacturing of FeCrCoMnNi high-entropy alloy: Effect of heat treatment on microstructure, residual stress and mechanical property. *J. Alloys Compd.* **2019**, *785*, 1144–1159. [CrossRef]
38. Laplanche, G.; Kostka, A.; Horst, O.M.; Eggeler, G.; George, E.P. Microstructure evolution and critical stress for twinning in the CrMnFeCoNi high-entropy alloy. *Acta Mater.* **2016**, *118*, 152–163. [CrossRef]
39. Zhang, C.; Feng, K.; Kokawa, H.; Han, B.; Li, Z. Cracking mechanism and mechanical properties of selective laser melted CoCrFeMnNi high entropy alloy using different scanning strategies. *Mater. Sci. Eng. A* **2020**, *789*, 139672. [CrossRef]
40. Zhang, D.; Kong, D. Microstructures and immersion corrosion behavior of laser thermal sprayed amorphous Al-Ni coatings in 3.5% NaCl solution. *J. Alloys Compd.* **2018**, *735*, 1–12. [CrossRef]
41. Fu, Z.; Yang, B.; Shan, M.; Li, T.; Zhu, Z.; Ma, C.; Zhang, X.; Gou, G.; Wang, Z.; Gao, W. Hydrogen embrittlement behavior of SUS301L-MT stainless steel laser-arc hybrid welded joint localized zones. *Corros. Sci.* **2020**, *164*, 108337. [CrossRef]
42. Kim, Y.-K.; Suh, J.-Y.; Lee, K.-A. Effect of gaseous hydrogen embrittlement on the mechanical properties of additively manufactured CrMnFeCoNi high-entropy alloy strengthened by in-situ formed oxide. *Mater. Sci. Eng. A* **2020**, *796*, 140039. [CrossRef]
43. Fu, Z.; Li, T.; Shan, M.; Gou, G.; Zhu, Z.; Ma, C.; Gao, W.; Hu, Y. Hydrogen atoms on the SCC behavior of SUS301L-MT stainless steel laser-arc hybrid welded joints. *Corros. Sci.* **2019**, *148*, 272–280. [CrossRef]
44. Kim, Y.-K.; Ham, G.-S.; Kim, H.S.; Lee, K.-A. High-cycle fatigue and tensile deformation behaviors of coarse-grained equiatomic CoCrFeMnNi high entropy alloy and unexpected hardening behavior during cyclic loading. *Intermetallics* **2019**, *111*, 106486. [CrossRef]
45. Dwivedi, S.K.; Vishwakarma, M. Hydrogen embrittlement in different materials: A review. *Int. J. Hydrog. Energy* **2018**, *43*, 21603–21616. [CrossRef]